

Effective field theory search for high-energy nuclear recoils using the XENON100 dark matter detector

E. Aprile,¹ J. Aalbers,² F. Agostini,^{3,4} M. Alfonsi,⁵ F. D. Amaro,⁶ M. Anthony,¹ F. Arneodo,⁷ P. Barrow,⁸ L. Baudis,⁸ B. Bauermeister,⁹ M. L. Benabderrahmane,⁷ T. Berger,¹⁰ P. A. Breur,² A. Brown,² E. Brown,¹⁰ S. Bruenner,¹¹ G. Bruno,³ R. Budnik,¹² L. Bütikofer,^{13,*} J. Calvén,⁹ J. M. R. Cardoso,⁶ M. Cervantes,¹⁴ D. Cichon,¹¹ D. Coderre,^{13,*} A. P. Colijn,² J. Conrad,^{9,†} J. P. Cussonneau,¹⁵ M. P. Decowski,² P. de Perio,¹ P. Di Gangi,⁴ A. Di Giovanni,⁷ S. Diglio,¹⁵ G. Eurin,¹¹ J. Fei,¹⁶ A. D. Ferella,⁹ A. Fieguth,¹⁷ W. Fulgione,^{3,18} A. Gallo Rosso,³ M. Galloway,⁸ F. Gao,¹ M. Garbini,⁴ C. Geis,⁵ L. W. Goetzke,¹ Z. Greene,¹ C. Grignon,⁵ C. Hasterok,¹¹ E. Hogenbirk,² R. Itay,^{12,‡} B. Kaminsky,^{13,*} S. Kazama,⁸ G. Kessler,⁸ A. Kish,⁸ H. Landsman,¹² R. F. Lang,¹⁴ D. Lellouch,¹² L. Levinson,¹² Q. Lin,¹ S. Lindemann,^{11,13} M. Lindner,¹¹ F. Lombardi,¹⁶ J. A. M. Lopes,^{6,§} A. Manfredini,^{12,||} I. Maris,⁷ T. Marrodán Undagoitia,¹¹ J. Masbou,¹⁵ F. V. Massoli,⁴ D. Masson,¹⁴ D. Mayani,⁸ M. Messina,¹ K. Micheneau,¹⁵ A. Molinaro,³ K. Morá,⁹ M. Murra,¹⁷ J. Naganoma,¹⁹ K. Ni,¹⁶ U. Oberlack,⁵ P. Pakarha,⁸ B. Pelsers,⁹ R. Persiani,¹⁵ F. Piastra,⁸ J. Pienaar,¹⁴ V. Pizzella,¹¹ M.-C. Piro,¹⁰ G. Plante,¹ N. Priel,¹² L. Rauch,¹¹ S. Reichard,¹⁴ C. Reuter,¹⁴ A. Rizzo,¹ S. Rosendahl,¹⁷ N. Rupp,¹¹ J. M. F. dos Santos,⁶ G. Sartorelli,⁴ M. Scheibelhut,⁵ S. Schindler,⁵ J. Schreiner,¹¹ M. Schumann,¹³ L. Scotto Lavina,²⁰ M. Selvi,⁴ P. Shagin,¹⁹ M. Silva,⁶ H. Simgen,¹¹ M. v. Sivers,^{13,*} A. Stein,²¹ D. Thers,¹⁵ A. Tiseni,² G. Trincherio,¹⁸ C. Tunnell,^{2,22} M. Vargas,¹⁷ H. Wang,²¹ Z. Wang,³ Y. Wei,⁸ C. Weinheimer,¹⁷ J. Wulf,⁸ J. Ye,¹⁶ and Y. Zhang,¹
(XENON Collaboration)[¶]

B. Farmer^{9,**}

¹Physics Department, Columbia University, New York, New York 10027, USA

²Nikhef and the University of Amsterdam, Science Park, 1098XG Amsterdam, Netherlands

³INFN-Laboratori Nazionali del Gran Sasso and Gran Sasso Science Institute, 67100 L'Aquila, Italy

⁴Department of Physics and Astrophysics, University of Bologna and INFN-Bologna, 40126 Bologna, Italy

⁵Institut für Physik & Exzellenzcluster PRISMA, Johannes Gutenberg-Universität Mainz, 55099 Mainz, Germany

⁶LIBPhys, Department of Physics, University of Coimbra, 3004-516 Coimbra, Portugal

⁷New York University Abu Dhabi, Abu Dhabi 129188, United Arab Emirates

⁸Physik-Institut, University of Zurich, 8057 Zurich, Switzerland

⁹Oskar Klein Centre, Department of Physics, Stockholm University, AlbaNova, Stockholm SE-10691, Sweden

¹⁰Department of Physics, Applied Physics and Astronomy, Rensselaer Polytechnic Institute, Troy, New York 12180, USA

¹¹Max-Planck-Institut für Kernphysik, 69117 Heidelberg, Germany

¹²Department of Particle Physics and Astrophysics, Weizmann Institute of Science, Rehovot 7610001, Israel

¹³Physikalisches Institut, Universität Freiburg, 79104 Freiburg, Germany

¹⁴Department of Physics and Astronomy, Purdue University, West Lafayette, Indiana 47907, USA

¹⁵SUBATECH, IMT Atlantique, CNRS/IN2P3, Université de Nantes, Nantes 44307, France

¹⁶Department of Physics, University of California, San Diego, California 92093, USA

¹⁷Institut für Kernphysik, Westfälische Wilhelms-Universität Münster, 48149 Münster, Germany

¹⁸INFN-Torino and Osservatorio Astrofisico di Torino, 10125 Torino, Italy

¹⁹Department of Physics and Astronomy, Rice University, Houston, Texas 77005, USA

²⁰LPNHE, Université Pierre et Marie Curie, Université Paris Diderot, CNRS/IN2P3, Paris 75252, France

²¹Physics & Astronomy Department, University of California, Los Angeles, California 90095, USA

²²Department of Physics & Kavli Institute of Cosmological Physics, University of Chicago, Chicago, Illinois 60637, USA

(Received 14 May 2017; published 31 August 2017)

* Also at Albert Einstein Center for Fundamental Physics, University of Bern, Bern, Switzerland.

† Wallenberg Academy Fellow.

‡ ran.itay@weizmann.ac.il

§ Also with Coimbra Engineering Institute, Coimbra, Portugal.

|| alessandro.manfredini@weizmann.ac.il

¶ xenon@lngs.infn.it

** benjamin.farmer@fysik.su.se

We report on weakly interacting massive particles (WIMPs) search results in the XENON100 detector using a nonrelativistic effective field theory approach. The data from science run II (34 kg \times 224.6 live days) were reanalyzed, with an increased recoil energy interval compared to previous analyses, ranging from (6.6–240) keV_{nr}. The data are found to be compatible with the background-only hypothesis. We present 90% confidence level exclusion limits on the coupling constants of WIMP-nucleon effective operators using a binned profile likelihood method. We also consider the case of inelastic WIMP scattering, where incident WIMPs may up-scatter to a higher mass state, and set exclusion limits on this model as well.

DOI: 10.1103/PhysRevD.96.042004

I. INTRODUCTION

Astrophysical and cosmological observations provide strong evidence that about 27% of the energy density of the Universe is DM, which is believed to be nonbaryonic, nonrelativistic, and nonluminous, but its exact nature is not fully known yet [1–3]. Many well-motivated theoretical extensions of the Standard Model of particle physics predict the existence of one or more particles with the required properties, with masses and cross sections typically of the order of the weak scale. Such particles are collectively known as weakly interacting massive particles (WIMPs) [4]. The hypothesis that dark matter is constituted primarily of WIMPs is currently being tested by many experiments, either indirectly by searching for evidence of their possible decay or annihilation in astrophysical processes, by searching for evidence of their direct production at collider experiments, or by directly measuring the rare scattering of astrophysical WIMPs from target nuclei in Earth-based laboratories [5–11]. We report on a search of this latter kind.

The traditional approach for computing predictions of the rate of WIMP-nucleon scattering has been to take only leading-order terms in a WIMP-nucleon effective field theory (EFT) with a very simple treatment of nuclear structure [12]. This leads to two main types of interactions, which are commonly labelled “spin independent” (SI) and “spin dependent” (SD). However, in recent years, many authors have pointed out that in certain theories these interactions may be suppressed or nonexistent, such that otherwise subleading interactions may dominate the scattering process [13]. To account for this possibility in a systematic way, a more sophisticated EFT approach has been developed [14–18]. In the new approach, an effective Lagrangian describing the WIMP-nucleus interaction is constructed, that takes into account all Galilean-invariant operators up to second order in the momentum exchange. This framework introduces new operators associated with different types of nuclear responses, along with the standard SI and SD ones, resulting in a set of 14 operators \mathcal{O}_i which may couple independently to protons and neutrons. In Eqs. (1), we list these operators following the convention from Ref. [17]. The operators depend explicitly on four linearly independent quantities: $\vec{v}^\perp \equiv \vec{v} + \frac{\vec{q}}{2\mu_N}$, the relative perpendicular velocity between the WIMP and the nucleon;

\vec{q} , the momentum transferred in the scattering event; and \vec{S}_χ and \vec{S}_N , the WIMP and nucleon spins. \mathcal{O}_2 is not considered here as it cannot be obtained from a relativistic operator at leading order,

$$\begin{aligned}
 \mathcal{O}_1 &= 1_\chi 1_N & \mathcal{O}_9 &= i\vec{S}_\chi \cdot \left(\vec{S}_N \times \frac{\vec{q}}{m_N} \right) \\
 \mathcal{O}_3 &= i\vec{S}_N \cdot \left(\frac{\vec{q}}{m_N} \times \vec{v}^\perp \right) & \mathcal{O}_{10} &= i\vec{S}_N \cdot \left(\frac{\vec{q}}{m_N} \right) \\
 \mathcal{O}_4 &= \vec{S}_\chi \cdot \vec{S}_N & \mathcal{O}_{11} &= i\vec{S}_\chi \cdot \left(\frac{\vec{q}}{m_N} \right) \\
 \mathcal{O}_5 &= i\vec{S}_\chi \cdot \left(\frac{\vec{q}}{m_N} \times \vec{v}^\perp \right) & \mathcal{O}_{12} &= \vec{S}_\chi \cdot (\vec{S}_N \times \vec{v}^\perp) \\
 \mathcal{O}_6 &= \left(\vec{S}_\chi \cdot \frac{\vec{q}}{m_N} \right) \left(\vec{S}_N \cdot \frac{\vec{q}}{m_N} \right) & \mathcal{O}_{13} &= i(\vec{S}_\chi \cdot \vec{v}^\perp) \left(\vec{S}_N \cdot \frac{\vec{q}}{m_N} \right) \\
 \mathcal{O}_7 &= \vec{S}_N \cdot \vec{v}^\perp & \mathcal{O}_{14} &= i \left(\vec{S}_\chi \cdot \frac{\vec{q}}{m_N} \right) (\vec{S}_N \cdot \vec{v}^\perp) \\
 \mathcal{O}_8 &= \vec{S}_\chi \cdot \vec{v}^\perp & \mathcal{O}_{15} &= - \left(\vec{S}_\chi \cdot \frac{\vec{q}}{m_N} \right) \left[(\vec{S}_N \times \vec{v}^\perp) \cdot \frac{\vec{q}}{m_N} \right].
 \end{aligned} \tag{1}$$

Unlike the more commonly studied types of interaction (SI and SD), which are not suppressed when $\vec{q} \rightarrow 0$ and for which the scattering rate on nucleons is expected to be largest for low energy nuclear recoils, some of the new EFT operators depend explicitly on \vec{q} , and so their interaction cross section is suppressed for low momentum transfers. Consequently, their scattering rate peaks at nonzero nuclear recoil energy. For sufficiently high WIMP masses, this may even occur outside typical analysis windows, which usually have an upper range of around 43 keV_{nr} (nuclear recoil equivalent energy) since they are designed to search for SI and SD interactions, which predict exponentially falling recoil spectra (see Fig. 1). Due to the theoretical bias of only considering SI and SD interactions, high energy nuclear recoils remain unexplored in many experiments.

Another typical assumption that can be relaxed is that WIMPs should scatter elastically with nuclei. There exist dark matter models in which the incoming and outgoing WIMPs have different mass states [19] separated by a keV-scale splitting. In the case where the outgoing state is more

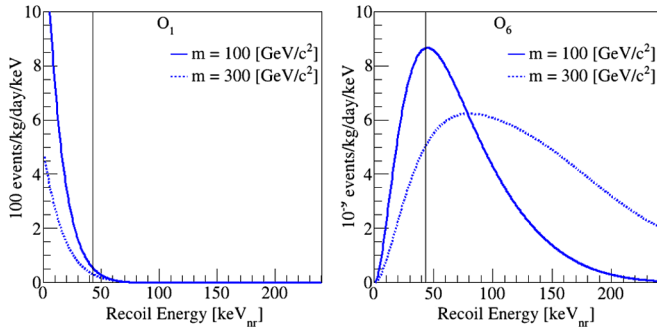


FIG. 1. Example EFT recoil spectra for elastic scattering of spin-1/2 WIMPs on xenon nuclei (weighted according to the isotope abundances in the XENON100 experiment). Left (right) shows the predicted spectra for EFT operator \mathcal{O}_1 (\mathcal{O}_6). The normalization is controlled by the coupling coefficient of each EFT operator and the experimental exposure. The solid vertical line at 43 keV_{nr} shows the approximate division between the two signal regions used in this analysis. As shown, the standard SI (\mathcal{O}_1) spectrum is concentrated mainly in the already explored energy region. However, some EFT operators, for certain WIMP masses, predict a significant fraction of recoil events above the upper energy cut used in the standard spin-independent analysis, motivating an extension of this cut. The highest recoil energy shown in the plots, 240 keV_{nr}, roughly corresponds to the highest energy accounted for this analysis.

massive than the incoming state, the cross section for low recoil energies can again be suppressed, this time by scattering kinematics. Recently, an inelastic adaptation of the EFT operator framework discussed above was developed [20]. In this case, the operators presented in Eqs. (1) are modified such that $\vec{v}_{\text{inelastic}}^\perp = \vec{v}_{\text{elastic}}^\perp + \frac{\delta_m}{|\vec{q}|^2} \vec{q}$. We consider this case in Sec. III C 2.

The EFT framework of Ref. [16] is constructed at the WIMP-nucleon level, and so each operator may be present independently for protons and neutrons, though UV models can of course correlate their couplings. The full EFT thus has 28 coupling parameters in addition to the WIMP mass, plus a mass splitting δ in the inelastic case. This parameter space is too large to explore in full, so we take a similar approach to the SI/SD case and assume only one active operator at a time, considering it equally coupled to protons and neutrons (the “isoscalar” case).

However, to facilitate the full exploitation of these results by the community, we provide in Supplemental Material [21] a set of tools for converting any theoretical recoil spectrum dR/dE into an accurate event rate prediction for this analysis, including all detector response and analysis efficiency effects. This may help to set a mildly conservative but quite accurate limit on arbitrary models in the full EFT parameter space, or any other particle dark matter model for which one can supply the expected recoil spectrum. These tools are described further in Appendix B.

Motivated by these EFT extensions of the standard WIMP framework, we report on an analysis extending

the searched recoil energy range up to 240 keV_{nr} for the first time in the XENON100 experiment and present exclusion limits on all operators for both elastic and inelastic WIMP cases.

II. XENON100 DETECTOR

The XENON100 detector is a cylindrical dual-phase xenon (liquid and gas) time projection chamber (TPC). It is installed at the Laboratori Nazionali del Gran Sasso in Italy and contains 161 kg of liquid xenon (LXe), of which 62 kg function as the active target [22]. The detector uses of a total of 178 1-in.² Hamamatsu R8520-AL photomultiplier tubes (PMTs) employed in two arrays, one in the gas phase at the top of the TPC and the other at the bottom, immersed in the LXe.

A particle interacting with the LXe deposits energy that creates both prompt scintillation (S1) and delayed proportional scintillation (S2) which are detected using the two PMT arrays. The S2 signal is produced by ionization electrons, drifted in an electric field of 530 V/cm toward the liquid-gas interface, where they are extracted to the gas phase using a stronger electric field of ~ 12 kV/cm in which the proportional scintillation occurs. The spatial distribution of the S2 signal on the top PMT array, together with the time difference between S1 and S2 signals, provide respectively x - y and z position information for each interaction, allowing 3D position reconstruction to be achieved.

Interaction in different locations of the detector have different signatures. In order to take these effects into account, a correction is applied based on light and charge collection efficiency maps. These maps are prepared using calibration sources ranging up to energies well above 240 keV_{nr}, which is the highest energy recoil considered in this paper. The corrected signals (cS1 and cS2_b) are spatially independent and uniform to all interactions [22]. Note that some of the top PMTs saturate for large S2 signals, and we therefore use in this analysis only the bottom PMT array to infer the energy scale in S2.

The S1/S2 ratio is known to differ between nuclear recoil (NR) and electronic recoil (ER) interactions and is thus used as a discriminating variable between a WIMP signal and ER background. The logarithm of this ratio, $\log(\text{cS2}_b/\text{cS1})$, is referred to later in the text as the discriminating “ y ” variable.

III. DATA ANALYSIS

In this work, we reanalyze science run II data recorded between February 2011 and March 2012, corresponding to 224.6 live days. The characterization of the detector response to ER interactions is performed using dedicated calibration campaigns with ⁶⁰Co and ²³²Th radioactive sources, while the response to NR interactions is performed using ²⁴¹AmBe neutron source calibration campaigns.

This work extends the previous results [5,23], referred to in the following as the low-energy channel, with a new study exploring the recoil energy range between (43–240) keV_{nr}. The data analysis is divided into two mutually exclusive channels, one optimized for low energies and ranging from (3–30) photoelectrons (PE) in cS1 (low energy) and the other optimized for high energies recoils ranging from (30–180) PE in cS1 (high energy). These two analyses are then combined statistically.

A. Low-energy channel

This analysis channel relies on the reanalysis of run II data described in Ref. [5]. The region of interest (ROI), background expectation models, data selections, and their acceptances are mostly unchanged and so are only briefly summarized here. Differences with respect to said results are highlighted when present.

The ROI for this channel is defined in the (y , cS1)-plane and is shown in Fig. 2. The lower bound on y corresponds to a 3σ acceptance quantile (as a function of cS1) of a 20 GeV WIMP mass signal model assuming an \mathcal{O}_1 (SI) interaction, while the upper bound is fixed at $y = 2.7$. The range in cS1 is selected as (3–30) PE. The ROI is further divided into eight subregions (also called bands) depending on the operator \mathcal{O}_i and on the WIMP mass hypothesis. These bands are arranged to achieve constant expected signal density in each region, as described in Ref. [5].

Other than falling into the ROI, an event should fulfill several additional selection criteria (cuts). Data quality and selection cuts are defined to remove events with poor data quality or noisy signals. Events are discarded if they present a time-coincident signal in the outer LXe veto, S2

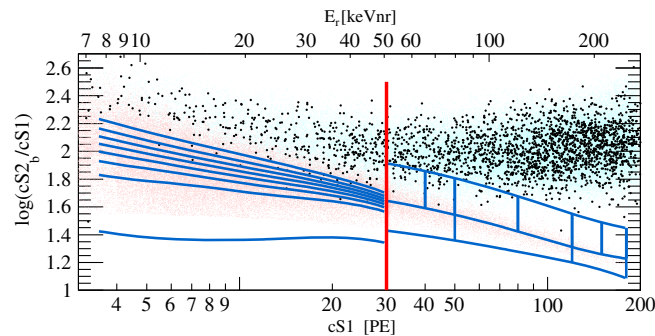


FIG. 2. Summary of regions of interest, backgrounds, and observed data. ER calibration data, namely ^{60}Co and ^{232}Th data, are shown as light cyan dots. NR calibration data ($^{241}\text{AmBe}$) are shown as light red dots. Dark matter search data are shown as black dots. The red line is the threshold between the low- and high-energy channels. The lines in blue are the bands. For the low-energy channel, the bands are constructed to achieve constant expected signal density and are operator and mass dependent, shown here for a 50 GeV/ c^2 WIMP using the \mathcal{O}_1 operator. For the high-energy region, the nine analysis bins are presented also in blue lines.

signals below threshold, multiple scatters or are localized outside a predefined fiducial volume of 34 kg. In addition, this analysis channel uses the postunblinding cuts and data reprocessing described in Ref. [5]. More details on these selection criteria and their relative WIMP signals acceptances can be found in Refs. [5,24].

Note that this analysis channel does not employ a variable lower S1 threshold as a function of the event position in the TPC but instead applies a fixed lower threshold cut on cS1 at 3 PE, conversely to the choice made in Ref. [5].

The expected background is modeled separately for ER and NR contributions which are then scaled to exposure and added together. The NR background is estimated by Monte Carlo simulation and accounts for the radiogenic and cosmogenic neutron contributions [25]. The ER background is parametrized as the linear combination of Gaussian-shaped and non-Gaussian components. The former is obtained via a parametric fit of the ^{60}Co and ^{232}Th calibration data, as discussed in Ref. [23].

The latter, which consist of anomalous events such as those presenting incomplete charge collection or accidental coincidence of uncorrelated S1s and S2s, is evaluated via dedicated techniques described in Ref. [5].

Systematic uncertainties on the background model arising from the Gaussian parametrized fit, and from the normalizations of the NR and non-Gaussian components, have been evaluated and propagated to each band. These errors are small with respect to the statistical uncertainties of each band, which are conservatively taken as the overall uncertainty [5], as discussed in Sec. III D.

B. High-energy channel

This analysis channel targets high-energy nuclear recoils and is the focus of this work. The data selection criteria used are based on the criteria described in detail in Ref. [24], which were optimized for high acceptance to low-energy nuclear recoils. Most of these cuts were found to be fully compatible with (or easily extended) to high-energy depositions; however, some required more comprehensive studies, which are described in the following.

The width of an S2 pulse increases with the depth (z) of the interaction. This is due to the diffusion of the electron cloud during its propagation through the liquid xenon. Since low-energy S2 events show larger spread due to low statistics of drifted electrons, the cut was previously defined in an energy-dependent way. However, for the large recoil energies considered in this channel, this energy dependency is no longer valid. We therefore use here a cut on the S2 width which is a function of the depth of the interaction alone.

As a WIMP will interact only once in the detector, we remove events which have more than one S2. We adopt in this analysis a cut that is more suitable to higher energies and demand a single S2 in a 160 μs window,

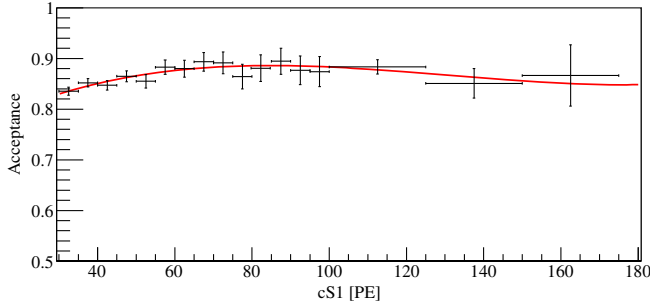


FIG. 3. The total acceptance of all cuts used. Data from calibration are shown in black, with a third-order polynomial fit in red.

instead of a linear dependence between the second S2 size and the first.

To define the interaction's exact location in (x, y) , we use several algorithms, one of which is based on a neural network (NN) [24]. The NN was not trained to recognize high-energy ER events, and therefore a cut on the NN reconstruction quality is not suitable for this analysis. We therefore discard this cut but keep all other selections on position reconstruction quality, which is sufficient to ensure a correct position reconstruction.

The total acceptance to WIMP signals is computed based on $^{241}\text{AmBe}$ calibration data as a function of cS1, following the procedure described in Ref. [24]. We present this function in Fig. 3, where the total acceptance is fitted using a third-order polynomial.

We define our signal region in the discrimination $(y, \text{cS1})$ -plane using $^{241}\text{AmBe}$ calibration data. The region of interest is shown in Fig. 2 as blue contour lines. The upper bound in y is defined such that the contribution due to xenon inelastic interaction lines is negligible. The lower bound is defined as the 3σ acceptance quantile of the $^{241}\text{AmBe}$ distribution.

We divide our signal region into two bands in y , constructed such that the $^{241}\text{AmBe}$ data sample is equally distributed between them. The number of events in each band is ~ 3000 . The bands are further divided into nine bins, the number and boundaries of which have been optimized via Monte Carlo simulation. The definitions of the bins boundaries are presented in Table I and in Fig. 2.

The main source of background results from ER leakage. We therefore estimate the background distribution in the ROI using ^{60}Co and ^{232}Th calibration events. Contributions from radiogenic and cosmogenic neutrons, as well as accidental coincidence, are negligible for such a high-energy recoil. In Table I, we report the background expectation in the ROI along with the observed events for each bin. Here, the background expectation is computed by scaling the calibration sample yield by 6.54×10^{-3} , which is the ratio of observed counts to calibration counts in an independent sideband. The sideband is defined above the upper limit of this analysis and below the ER

TABLE I. Definitions and contents of the analysis bins for the high-energy channel. The expected background counts are calculated by taking the calibration sample and scaling it by 6.54×10^{-3} , which is the ratio of observed counts to calibration counts in a sideband.

Number	Band	Energy range (cS1)	Number Background events	Number Data events
1	Upper	30–40	24 ± 5	20
2	Upper	40–50	16 ± 3	17
3	Upper	50–80	12 ± 3	11
4	Upper	80–120	1.1 ± 0.3	1
5	Upper	120–150	$(1.0 \pm 0.5) \times 10^{-1}$	1
6	Upper	150–180	$(0.8 \pm 0.4) \times 10^{-1}$	0
7	Lower	30–50	0.9 ± 0.3	0
8	Lower	50–90	$(3.5 \pm 1.2) \times 10^{-1}$	0
9	Lower	90–180	$(1.8 \pm 0.7) \times 10^{-1}$	0

calibration band mean. Note that in the computation of exclusion limits the background normalization is fitted to data, rather than using the sideband normalization, as described in Sec. III D.

C. Signal model

The signal model is produced by taking a theoretical event rate spectrum, the production of which is described in Secs. III C 1 and III C 2 and applying the analysis acceptance and detector response as described in Ref. [24] to obtain the expected event rate in the detector in terms of detector variables (i.e., cS1 and cS2_b). In both analysis channels, we use Eq. (2) in order to compute the expected average cS1 for a given NR energy,

$$\langle \text{cS1} \rangle = E_{\text{nr}} \cdot (L_y \mathcal{L}_{\text{eff}}) \cdot \left(\frac{S_{\text{nr}}}{S_{\text{ee}}} \right), \quad (2)$$

where E_{nr} is the recoil energy, L_y is the average light yield in the detector, \mathcal{L}_{eff} is the scintillation efficiency relative to 122 keV_{ee} as a function of E_{nr} , and S_{ee} and S_{nr} are the quenching factors due to the externally applied electric field. Aside from E_{nr} and \mathcal{L}_{eff} , these parameters have fixed values, namely $L_y = 2.28 \pm 0.04$, $S_{\text{nr}} = 0.95$, and $S_{\text{ee}} = 0.58$. Recoils below 3 keV_{nr} are assumed to produce no light. For details of the physics behind these parameters and the construction of the signal probability density function (PDF), please see Refs. [5,24].

For the low-energy region, the expected cS2_b signal is computed following Ref. [26] using Eq. (3),

$$\langle \text{cS2}_b \rangle = E_{\text{nr}} Q_y Y, \quad (3)$$

where $Y = 8.3 \pm 0.3$ is the amplification factor determined from the detector response to single electrons [27] and Q_y is the charge yield as a function of E_{nr} . Applying the

detector and PMT responses, and the acceptance as in Ref. [5], defines the low-energy signal model over the region $3 \text{ PE} < \text{cS1} < 30 \text{ PE}$, with $\text{cS2}_b > 73.5 \text{ PE}$ as the S2 threshold.

Equation (3) hides a subtlety. The actual cS2_b PDF is composed of two pieces, a Poisson term associated with the initial charge liberation, and a Gaussian term associated with the PMT response and other detector effects,

$$p_{\text{S2}}(\text{cS2}_b|E) = \sum_{N'} P_{\text{pmt}}(\text{cS2}_b|YN', \sigma_Y \sqrt{N'}) \cdot \text{Pois}(N'|\mu_Q), \quad (4)$$

where $\mu_Q = E_{\text{nr}} Q_y$ is the expected number of liberated charges in a nuclear recoil event of energy E and N' is the actual number of liberated charges. The amplification factor Y is applied to the actual number of liberated charges N' , not the expected number μ_Q . Associated with this is the variance of the Gaussian response PDF, $\sigma_Y \sqrt{N'}$, where in this analysis $\sigma_Y = 6.93$ as measured and described in Ref. [27].

For the high-energy region, we cannot produce the S2 distribution in the same way as the method in Ref. [26], since it has not been calibrated for such high recoil energies. We therefore use the NR calibration data distribution in $\log(\text{cS2}_b/\text{cS1})$ to estimate the WIMP distribution. Above 180 PE in cS1, the event yield of $^{241}\text{AmBe}$ data is too low to estimate the distribution accurately. This forms the upper bound of this analysis. With the cS2_b distribution determined by this empirical method, we require only a prediction of the cS1 distribution. This is obtained from Eq. (2), followed by the application of detector and PMT responses, as well as the acceptance given in Figure. 3, which completes the high-energy signal model definition.

Figures 4 and 5 show signal distribution examples for two EFT operators and for the low- and the high-energy region, respectively. In both cases, the signal distributions

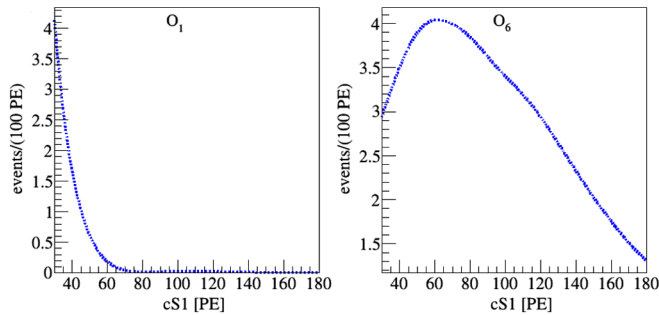


FIG. 4. The expected signal in the high-energy region for a $300 \text{ GeV}/c^2$ WIMP mass, normalized to five events. Left (right) is the spectra for O_1 (O_6). Notice that for O_1 most of the events are not expected to deposit energy higher than 30 PE, whereas for O_6 , a large fraction of the events appear in this region.

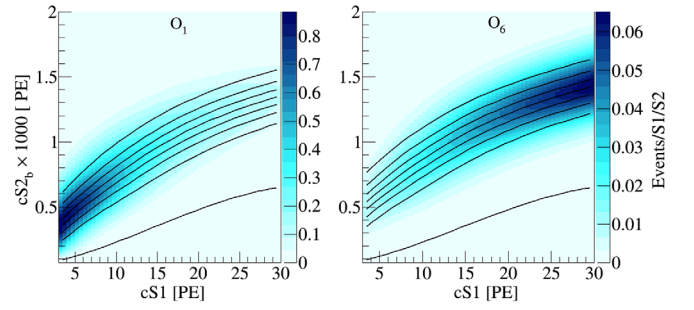


FIG. 5. The expected signal in the low-energy region for a $300 \text{ GeV}/c^2$ WIMP mass, normalized to five events. Left (right) is the spectra for O_1 (O_6). Notice that for O_1 most of the events are expected to deposit energy lower than 30 PE, whereas for O_6 , a large fraction of the events do not appear in this region at all. The black lines indicate the bands constructed on these specific mass and operator models and are dividing the signal into eight equally distributed signal subregions. This parameter space can be mapped with a one-to-one mapping to the $(y - \text{cS1})$ space.

are normalized to yield five events in the total energy range (low energy and high energy).

1. Elastic scattering

The expected recoil energy spectrum of each WIMP mass for each EFT operator is calculated using the *Mathematica* package *DMForm Factor* supplied by Anand *et al.* [17,18]. We use standard assumptions as in previous analyses (e.g. Ref. [5]) regarding the local dark matter density and velocity distribution, namely $\rho_{\text{local}} = 0.3 \text{ GeV} \cdot c^{-2}/\text{cm}^3$ and a Maxwell-Boltzman distribution with a mean given by the local circular velocity $v_0 = 220 \text{ km/s}$ and cut off at an escape velocity of $v_{\text{esc}} = 544 \text{ km/s}$. The responses of xenon nuclei to a scattering event are computed from one-body density matrices provided with the package, in contrast to the Helm form factors which have been used in previous analyses. These spectra are produced for the seven most abundant xenon isotopes (128, 129, 130, 131, 132, 134, and 136), combined in proportion to the abundance of these isotopes in the XENON detector [28], then translated into expected signal rates via the method described above.

2. Inelastic WIMP scattering

To obtain recoil spectra for WIMP-nucleon scattering for all EFT operators with inelastic kinematics, we use a modified version of *DMForm Factor* provided by Barello *et al.* [20]. The authors have modified the original package to enforce the new energy conservation condition $\delta_m + \vec{v} \cdot \vec{q} + |\vec{q}|^2/2\mu_N = 0$, primarily by replacing $\vec{v}_{\text{elastic}}^\perp \rightarrow \vec{v}_{\text{inelastic}}^\perp = \vec{v}_{\text{elastic}}^\perp + \frac{\delta_m}{|\vec{q}|^2} \vec{q}$ in the definitions of the EFT and nuclear operators, giving rise to the well-known minimum velocity for scattering

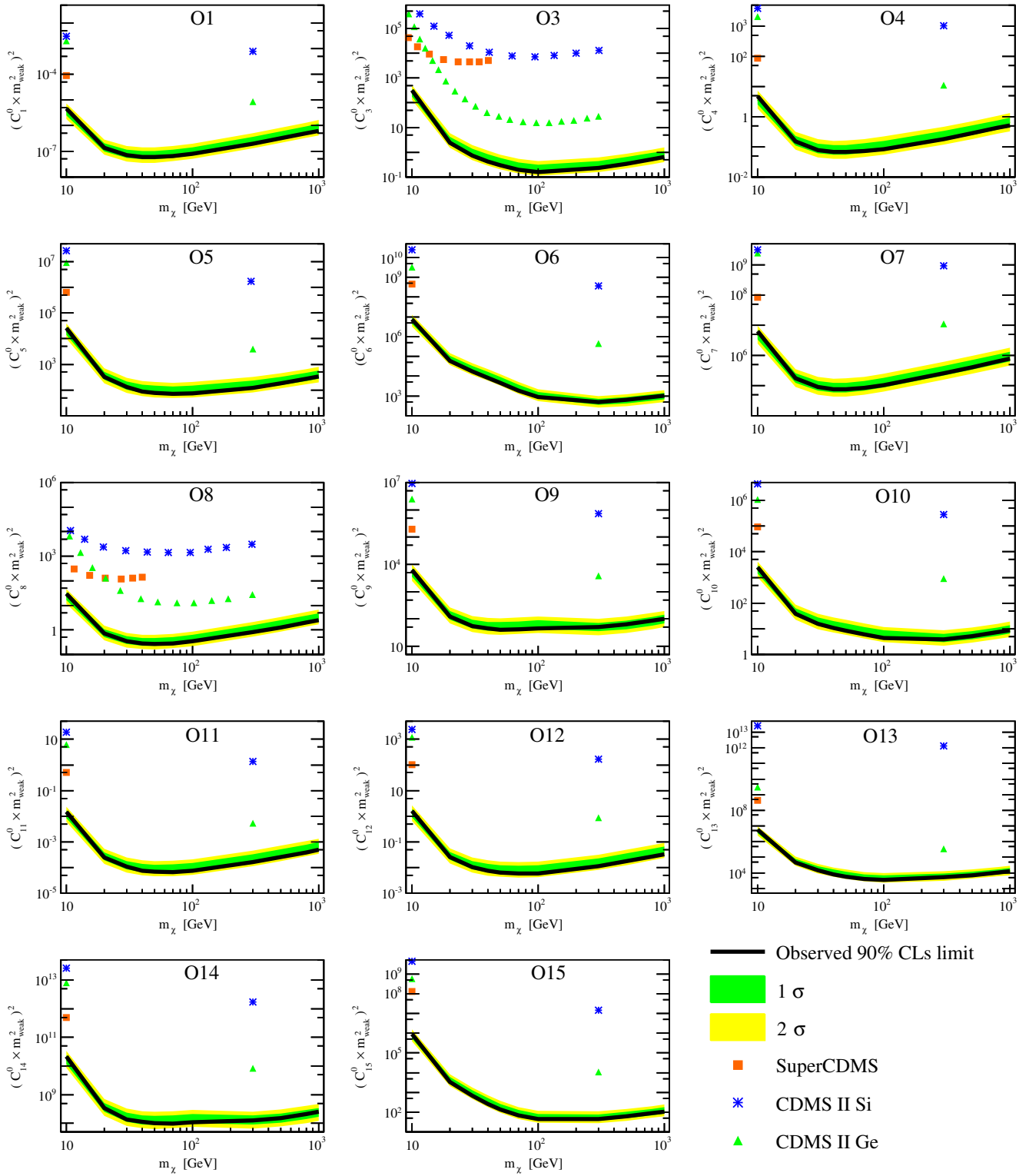


FIG. 6. The XENON100 limits (90% C.L.) on isoscalar dimensionless coupling for all elastic scattering EFT operators. The limits are indicated in solid black. The expected sensitivity is shown in green and yellow (1 σ and 2 σ , respectively). Limits from CDMS-II Si, CDMS-II Ge, and SuperCDMS [33] are presented as blue asterisks, green triangles, and orange rectangles, respectively. For operators 3 and 8, a full limit was published, for all other operators only $m_\chi = 10$ and $m_\chi = 300$ are available.

$$v_{\min}/c = \frac{1}{\sqrt{2m_N E_R}} \left| \frac{m_N E_R}{\mu_N} + \delta_m \right|, \quad (5)$$

where μ_N is the WIMP-nucleon reduced mass.

Assumptions regarding the dark matter halo and nuclear physics are unchanged. The mass splitting δ_m between dark matter states is varied from (0–300) keV, safely beyond the value at which the predicted rate is zero for the entire mass range we consider.

D. Statistical inference

The statistical interpretation of data is performed using a binned profile likelihood method, in which hypothesis testing relies upon a likelihood ratio test statistic, \tilde{q} , and its asymptotic distributions [29]. The two analysis channels are combined by multiplying their likelihoods together to produce a joint likelihood. Both analyses parametrize the NR relative scintillation efficiency, \mathcal{L}_{eff} , based on existing measurements [30]. Its uncertainty is the major contributor to energy scale uncertainties and is considered as correlated between the two analysis channels via a joint nuisance likelihood term. Throughout this study, all the parameters related to systematic uncertainties are assumed to be normally distributed.

For the low-energy channel, an extended likelihood function, which is very similar to the one reported in Ref. [31] and described in detail in Ref. [5], is employed. The $(y, \text{cS1})$ -plane is divided into eight WIMP mass-dependent bands where events are counted. This binned approach is extended with the corresponding cS1-projected PDF of each band. The total normalization of the background is fit to data, and an uncertainty is assigned to the relative normalization of each band according to the corresponding statistical uncertainty of the calibration sample. Signal shape variations due to energy scale uncertainty are modeled via simulation. These include the said \mathcal{L}_{eff} uncertainties and additionally the charge yield uncertainties, which are parametrized based on Q_y measurement as described in Ref. [26].

The high-energy channel analysis employs a binned likelihood function. Observed and expected event yield are compared in the nine ROI $(y, \text{cS1})$ bins described in Sec. III B. Given the large statistical uncertainty of the background model, the above extended likelihood approach is not repeated here. Instead, the maximum likelihood estimation of the background expectation in each bin is constrained by the statistical uncertainty of the calibration sample, while the total normalization is fit to the data. Additionally, to account for potential mismodeling of the expected background distribution, mainly due to anomalous multiple scatter events, a systematic uncertainty of 20% is assigned independently to each bin. In the high-energy channel, uncertainty on the signal acceptance of analysis selections are computed for each signal hypothesis using the parametrized acceptance curve shown in

Fig. 3. Uncertainties on the signal model $(y, \text{cS1})$ distribution due to $^{241}\text{AmBe}$ sample statistical fluctuations, as well as energy scale shape variation due to \mathcal{L}_{eff} uncertainties, are taken into account.

IV. RESULTS

A benchmark region of interest is defined between the upper and lower thresholds in cS1 for each channel. This region is bounded in y -space from above by the $^{241}\text{AmBe}$ NR mean line and below by the lower 3σ quantile of the $^{241}\text{AmBe}$ neutron calibration data. The expected background in the region is $3.0 \pm 0.5_{\text{stat}}$ (low energy) and $1.4 \pm 0.3_{\text{stat}}$ (high energy). The number of DM candidates in this benchmark region is 3 (low energy) and 0 (high energy). Consequently, the data are compatible with the background-only hypothesis, and no excess is found.

For the elastic scattering case, a 90% C.L._s [32] limit is set on the effective coupling constant, c_i , for all operators and masses in the range of 10 GeV/ c^2 to 1 TeV/ c^2 . The c_i are dimensional, with units of [mass]⁻², so we first convert them to dimensionless quantities by multiplying them by $m_{\text{weak}}^2 = (246.2 \text{ GeV})^2$, following the conventions of Ref. [17].

These limits are shown in Fig. 6 in black, along with limits from CDMS-II Si, CDMS-II Ge, and SuperCDMS [33].

For the inelastic scattering case, 90% C.L._s limits on the coupling constant as a function of mass splitting and WIMP mass for interaction operator \mathcal{O}_1 , are shown in Fig. 7. Limits on the coupling constants of all interaction operators for a WIMP with mass of 1 TeV, are shown in Fig. 8, projections of results from CDMS-II [34], ZEPLIN-III [35], and XENON100 [36] in the coupling constant and δ_m parameter space are also reported.

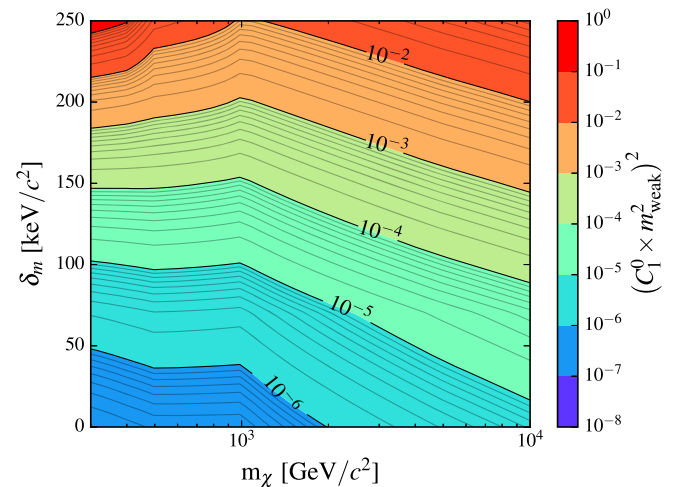


FIG. 7. 90% C.L._s limits, for the inelastic model, on the magnitude of the coupling constant for \mathcal{O}_1 , reported as a function of the WIMP mass and mass splitting δ .

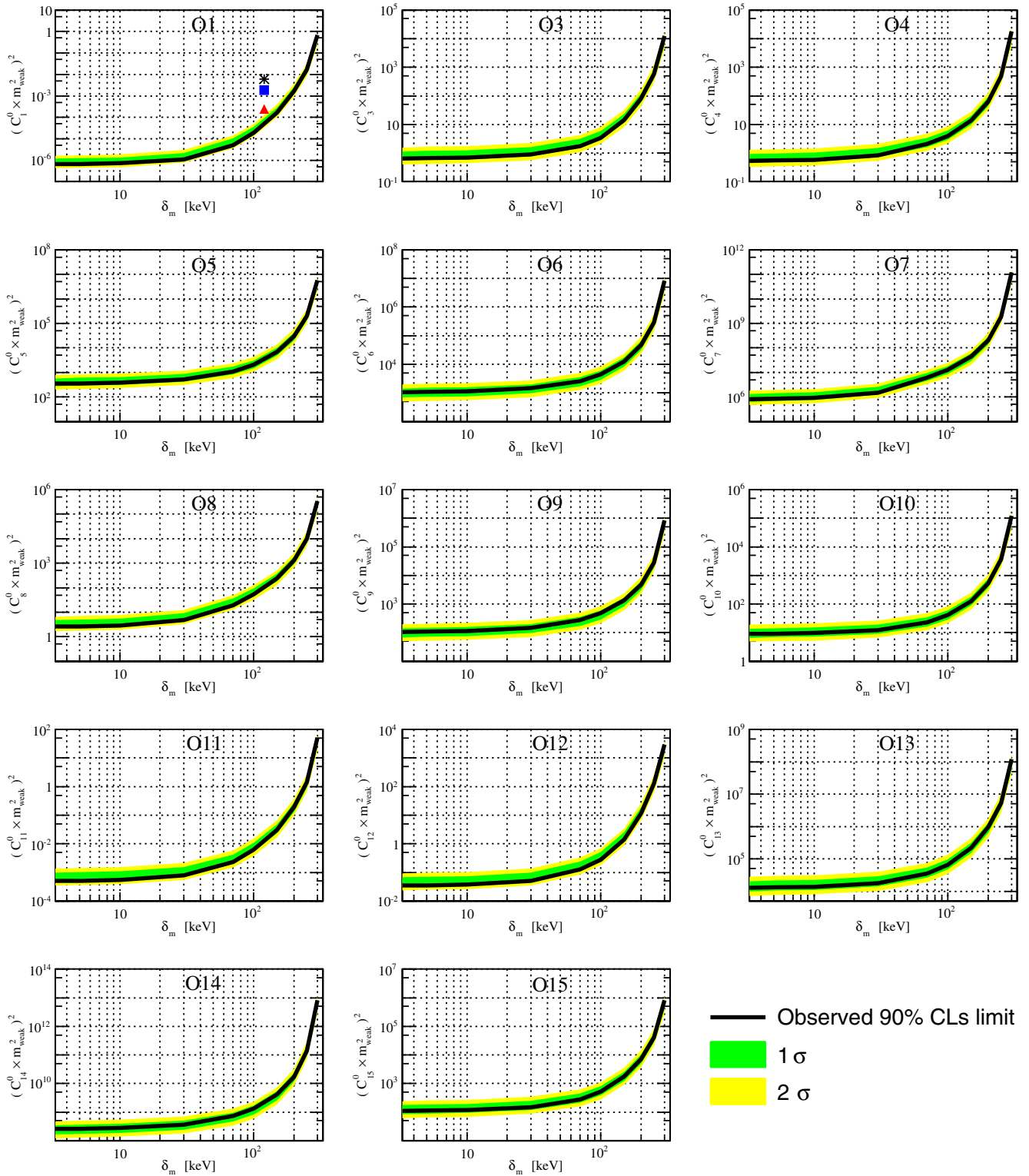


FIG. 8. The XENON100 90%CL_s limits on a 1 TeV/ c^2 WIMP isoscalar dimensionless coupling constant as a function of the WIMP mass splitting δ_m for all inelastic scattering EFT operators. Limits are indicated in solid black. The expected sensitivity is shown in green and yellow (1σ and 2σ , respectively). For \mathcal{O}_1 , (SI) results from XENON100 (red triangle), CDMS-II (blue rectangle), and ZEPLIN-III (black star) are overlaid.

For the elastic operator O_1 , our results can be compared to those of standard SI analyses by computing the relevant zero-momentum WIMP-nucleon cross sections. This is not simple to do rigorously because the treatment of nuclear structure used in our analysis is different than in standard analyses; however, this difference is small for scattering via O_1 . We can therefore quite safely use the “traditional” correspondence [37]

$$\sigma_N^{\text{SI}} = (C_1^N)^2 \frac{\mu_{\chi,N}^2}{\pi}, \quad (6)$$

where $\mu_{\chi,N}$ is the WIMP-nucleon reduced mass. Standard SI analyses assume isospin-conserving interactions, as we do in this analysis, so we can simply set $C_1^N = C_1^0$, such that $\sigma_p^{\text{SI}} = \sigma_n^{\text{SI}}$.

In principle, a similar comparison can be done between our limit on the O_4 coupling and standard SD analysis limits; however, this time, the standard analyses do *not* assume isospin-conserving interactions. Instead, they typically assume maximal isospin violation, that is, assuming that WIMPs couple either protons or neutrons. Limits are then derived independently on σ_p^{SD} and σ_n^{SD} . Because of this difference in assumptions, our limits on SD couplings are not directly comparable to usual analyses. However, they can be recast under the appropriate alternate model assumptions using the detector response tables we provide in the supplemental material [21].

V. SUMMARY

We have shown the first analysis of XENON100 data at recoil energies above 43keV_{nr} , with the new high-energy bound set to $240\text{keV}_{\text{nr}}$. We considered in this paper two models which predict interactions in this energy region: an EFT approach for elastic WIMP-nucleon scattering and a similar EFT approach but considering instead inelastic WIMP-nucleon scattering. The observed data were compatible with background expectations, and 90%C.L._s exclusion limits were constructed for WIMP masses between (10 and 1000) GeV.

ACKNOWLEDGMENTS

We would like to thank Andrew Liam Fitzpatrick and Spencer Chang for supplying and helping with their *Mathematica* packages. We gratefully acknowledge support from the National Science Foundation, Swiss National Science Foundation, Deutsche Forschungsgemeinschaft, Max Planck Gesellschaft, German Ministry for Education and Research, Netherlands Organisation for Scientific Research, Weizmann Institute of Science, I-CORE, Initial Training Network Invisibles (Marie Curie Actions, Grant No. PITNGA-2011-289442), Fundacao para a Ciencia e a Tecnologia, Region des Pays de la Loire, Knut and Alice Wallenberg Foundation, Kavli Foundation, and Istituto

Nazionale di Fisica Nucleare. We are grateful to Laboratori Nazionali del Gran Sasso for hosting and supporting the XENON project.

APPENDIX A: DATA FROM RECOIL ENERGIES UP TO 1000 PE

Upon completing our analysis, we examined data in the cS1 region above 180 PE, up to 1000 PE, since it will not be analyzed in any future XENON publications. We used the same data selection criteria as those applied for the high-energy channel. These selection criteria are not optimized for the new even-higher energies and may exhibit a drop in acceptance for NRs to below 50%. Due to the lack of NR calibration data and of a rigorous background model in this energy range, a quantitative and statistically solid inference on dark matter hypotheses is impractical. Nonetheless, we provide a plot of the data here. Figure 9 shows the distribution of science data in this extended range (in black) together with NR (in red) and ER calibration data (in blue).

The NR calibration data show the NR band from elastic scattering, with the aforementioned loss of statistics at energies above 180 PE clearly visible. Also visible are lines in the ER band from the inelastic scattering of neutrons on ^{129}Xe (39.6 keV at 130 PE) and ^{131}Xe (80.2 keV at 220 PE) as well as the delayed deexcitation of ^{131m}Xe (169.3 keV at 350 PE) and ^{129m}Xe (236.1 keV at 500 PE). ER calibration data are shown in blue and indicate the distribution of the prevalent background in this energy range. Since the detector is optimized for low-energy events, large S2 pulses saturate the PMT bases. This is visible in the ER band above 250 PE.

Finally, data from the dark matter search are shown in black. As can be seen, there is no indication of elastic NRs at energies above those analyzed in this study.

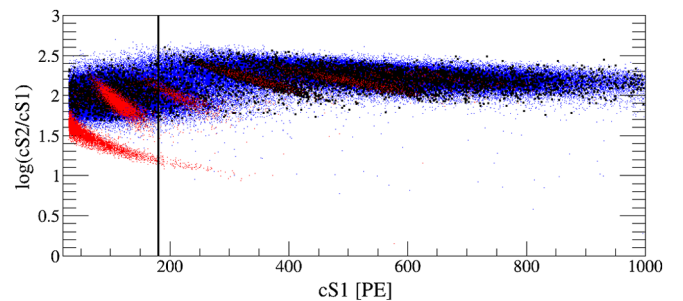


FIG. 9. The full XENON100 dark matter science run data up to 1000 PE in cS1 (shown in black). In blue, we show data from ER calibration (^{60}Co and ^{232}Th), and in red, we show data from NR calibration ($^{241}\text{AmBe}$). See the text for details on these populations. While the black vertical line represents the highest energy considered for quantitative interpretation in this analysis, there is no indication of elastic NRs even above that energy.

APPENDIX B: SIGNAL MODEL DETECTOR RESPONSE TABLE

In this Appendix, we describe digital tables which can be used to construct an accurate signal model for this analysis given any input recoil spectrum dR/dE arising from a theoretical model. A visualization of the tables is shown in Fig. 10, and in Appendix B 1, we show a simple example Python code of how to use the supplied tables. Currently, we provide these tables only for the high-energy analysis region.

The signal model for the high-energy analysis region can be expressed analytically in the form

$$\frac{dR}{dcS1} = \int \frac{dR}{dE} \cdot \epsilon_{S1}(cS1) \cdot \epsilon_{S2'}(E) \cdot p_{S1}(cS1|E) dE \quad (B1)$$

$$= \int \frac{dR}{dE} G(cS1, E) dE, \quad (B2)$$

where $\epsilon_{S1}(cS1)$ and $\epsilon_{S2'}(E)$ represent analysis cut efficiencies, $p_{S1}(cS1|E)$ encodes detector effects, and dR/dE gives the theoretically predicted nuclear recoil rate from WIMP scattering. In the second line, we emphasize that all the detector and analysis effects can be encoded in a single function $G(cS1, E)$. To make a signal prediction for the bins in our analysis, this expression needs to be integrated over the appropriate range of $cS1$ for each bin (and divided by 2 to account for the banding structure in $cS2_b$):

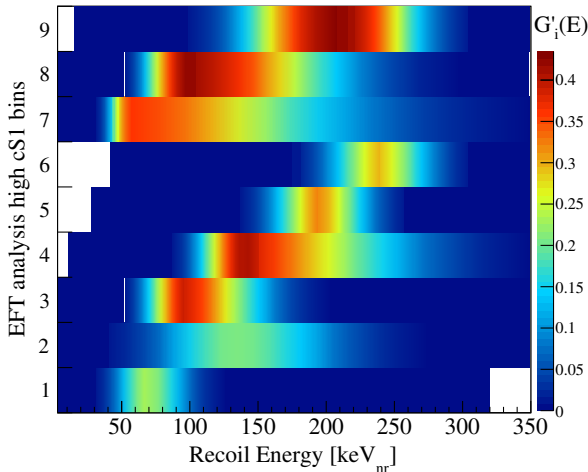


FIG. 10. A visualization of the detector response table for -1σ (i.e., conservative) \mathcal{L}_{eff} , as provided in the supplemental material [21]. The y axis indicates the bins used for the high-energy signal region of this analysis (explained in Table I). The x axis shows recoil energies, and the colors give the probability density for a recoil of a given recoil energy to produce an event in each analysis bin. To produce a signal model for this analysis, one simply multiplies the table values by dR/dE and integrates over E . The result is the predicted signal rate for each analysis bin.

$$R_{\text{bin}_i} = \frac{1}{2} \int_{\text{lower}_i}^{\text{upper}_i} \frac{dR}{dcS1} dcS1. \quad (B3)$$

With some simple rearrangement, this rate can be written in terms of an integral over the detector response function G as follows,

$$R_{\text{bin}_i} = \frac{1}{2} \int \frac{dR}{dE} \int_{\text{lower}_i}^{\text{upper}_i} G(cS1, E) dcS1 dE \quad (B4)$$

$$= \int \frac{dR}{dE} G'_i(E) dE, \quad (B5)$$

where in the last line we absorb the factor of $1/2$ into the definition of G'_i . We see here that the signal rate for each bin can be expressed as an integral over the recoil spectrum times a detector response function G'_i for that bin. It is these detector response functions which are shown in Fig. 10 and which we provide digitally for use by the community. A low-resolution example is given in Table II. With these tables, it is simple to produce a signal model for our analysis for any theoretical recoil spectrum. The functions G'_i are provided for three values of the nuisance variable \mathcal{L}_{eff} , namely, the median value and values at $\pm 1\sigma$ in \mathcal{L}_{eff} . From these, along with the measured background rates given in Table I, one may construct a likelihood which accounts for uncertainties in \mathcal{L}_{eff} . Alternatively, simply using the -1σ value produces quite an accurate prediction and is generally conservative.

1. Example code

```
import numpy as np
from numpy import newaxis
from scipy.interpolate import interp1d

def TrapI(x, y):
    """Simple trapezoid integration"""
    w=x[1:]-x[:-1]
    h=(y[1:]+y[:-1])/2.
    return np.sum(w*h,axis=0)

#Load detector response table
data=np.loadtxt("etector_table.dat")
E=data[:,0]; Gi=data[:,1:]
# Load test recoil spectrum (1 TeV WIMP, O6)
data=np.loadtxt("O6_1 TeV.dat")
Er=data[:,0]
# Input spectra is normalised to
coupling^2=1,
# rescale to something near limit (1e3)
# Also multiply in the appropriate
exposure
```

TABLE II. Detector response table using \mathcal{L}_{eff} with constrained scaling parameter set to a -1σ value. The first column gives recoil energies, and subsequent columns give the values of $G'_i(E)$ for each of the nine high-energy analysis bins. The sampling is in steps of $10 \text{ keV}_{\text{nr}}$, which is too coarse to give an accurate signal model for very low WIMP masses, but is suitable for the mass range most relevant to our analysis. Higher resolution $G'_i(E)$ functions, and $G'_i(E)$ functions for other values of \mathcal{L}_{eff} , are given in the Supplemental Material [21].

Number E (keV)	Bin 1	Bin 2	Bin 3	Bin 4	Bin 5	Bin 6	Bin 7	Bin 8	Bin 9
3.00e+00	1.44e-22	2.70e-32	1.23e-42	0.00e+00	0.00e+00	0.00e+00	1.44e-22	1.23e-42	0.00e+00
1.30e+01	9.21e-09	7.58e-14	1.25e-19	6.21e-40	0.00e+00	0.00e+00	9.21e-09	1.25e-19	0.00e+00
2.30e+01	1.74e-04	1.07e-07	1.24e-11	1.51e-26	0.00e+00	0.00e+00	1.74e-04	1.24e-11	2.64e-32
3.30e+01	2.22e-02	2.79e-04	6.56e-07	5.47e-18	8.20e-38	0.00e+00	2.25e-02	6.56e-07	1.71e-22
4.30e+01	1.59e-01	1.68e-02	3.50e-04	1.89e-12	1.24e-28	1.82e-43	1.76e-01	3.50e-04	4.95e-16
5.30e+01	2.23e-01	1.21e-01	1.40e-02	1.28e-08	6.89e-22	1.43e-34	3.44e-01	1.40e-02	1.82e-11
6.30e+01	1.10e-01	2.12e-01	9.84e-02	4.73e-06	5.28e-17	5.47e-28	3.21e-01	9.84e-02	2.59e-08
7.30e+01	2.77e-02	1.54e-01	2.51e-01	2.58e-04	2.20e-13	5.56e-23	1.82e-01	2.51e-01	4.20e-06
8.30e+01	4.38e-03	6.14e-02	3.67e-01	4.07e-03	1.36e-10	5.26e-19	6.58e-02	3.71e-01	1.65e-04
9.30e+01	4.65e-04	1.52e-02	3.96e-01	2.73e-02	2.31e-08	1.01e-15	1.57e-02	4.21e-01	2.44e-03
1.03e+02	3.40e-05	2.47e-03	3.41e-01	9.81e-02	1.50e-06	6.05e-13	2.50e-03	4.21e-01	1.75e-02
1.13e+02	1.91e-06	2.89e-04	2.29e-01	2.13e-01	4.09e-05	1.22e-10	2.91e-04	3.74e-01	6.77e-02
1.23e+02	7.75e-08	2.38e-05	1.14e-01	3.28e-01	5.91e-04	1.16e-08	2.39e-05	2.76e-01	1.66e-01
1.33e+02	2.18e-09	1.33e-06	3.98e-02	3.97e-01	5.03e-03	5.94e-07	1.33e-06	1.55e-01	2.87e-01
1.43e+02	5.40e-11	6.21e-08	1.05e-02	4.06e-01	2.41e-02	1.42e-05	6.21e-08	6.64e-02	3.74e-01
1.53e+02	1.33e-12	2.71e-09	2.23e-03	3.66e-01	7.14e-02	1.73e-04	2.71e-09	2.26e-02	4.17e-01
1.63e+02	2.86e-14	1.00e-10	3.75e-04	2.85e-01	1.51e-01	1.32e-03	1.00e-10	6.04e-03	4.32e-01
1.73e+02	5.43e-16	3.19e-12	5.09e-05	1.86e-01	2.43e-01	6.76e-03	3.19e-12	1.28e-03	4.34e-01
1.83e+02	9.29e-18	8.90e-14	5.69e-06	1.01e-01	3.09e-01	2.42e-02	8.90e-14	2.21e-04	4.34e-01
1.93e+02	1.44e-19	2.21e-15	5.32e-07	4.46e-02	3.23e-01	6.38e-02	2.21e-15	3.14e-05	4.31e-01
2.03e+02	2.05e-21	4.92e-17	4.23e-08	1.62e-02	2.83e-01	1.29e-01	4.92e-17	3.73e-06	4.28e-01
2.13e+02	2.71e-23	9.96e-19	2.91e-09	4.89e-03	2.10e-01	2.06e-01	9.96e-19	3.78e-07	4.21e-01
2.23e+02	3.33e-25	1.85e-20	1.74e-10	1.23e-03	1.31e-01	2.71e-01	1.85e-20	3.29e-08	4.04e-01
2.33e+02	3.83e-27	3.16e-22	9.25e-12	2.63e-04	6.94e-02	2.99e-01	3.16e-22	2.51e-09	3.69e-01
2.43e+02	4.16e-29	5.03e-24	4.38e-13	4.80e-05	3.12e-02	2.81e-01	5.03e-24	1.68e-10	3.12e-01
2.53e+02	4.29e-31	7.48e-26	1.87e-14	7.55e-06	1.20e-02	2.27e-01	7.48e-26	1.00e-11	2.39e-01
2.63e+02	4.21e-33	1.05e-27	7.23e-16	1.04e-06	3.94e-03	1.58e-01	1.05e-27	5.38e-13	1.62e-01
2.73e+02	3.95e-35	1.39e-29	2.56e-17	1.25e-07	1.12e-03	9.59e-02	1.39e-29	2.61e-14	9.70e-02
2.83e+02	3.56e-37	1.74e-31	8.33e-19	1.34e-08	2.77e-04	5.04e-02	1.74e-31	1.15e-15	5.07e-02
2.93e+02	3.08e-39	2.08e-33	2.51e-20	1.29e-09	6.00e-05	2.31e-02	2.08e-33	4.67e-17	2.31e-02
3.03e+02	2.58e-41	2.38e-35	7.04e-22	1.11e-10	1.15e-05	9.25e-03	2.38e-35	1.75e-18	9.26e-03
3.13e+02	2.03e-43	2.61e-37	1.84e-23	8.69e-12	1.95e-06	3.26e-03	2.61e-37	6.06e-20	3.26e-03
3.23e+02	0.00e+00	2.76e-39	4.54e-25	6.20e-13	2.97e-07	1.01e-03	2.76e-39	1.96e-21	1.01e-03
3.33e+02	0.00e+00	2.81e-41	1.05e-26	4.06e-14	4.06e-08	2.80e-04	2.81e-41	5.93e-23	2.80e-04
3.43e+02	0.00e+00	2.72e-43	2.32e-28	2.44e-15	5.04e-09	6.91e-05	2.72e-43	1.69e-24	6.91e-05

```

dRdE=data[:,1] * (1e3/1.) * 224.6*34.      Output :
# Interpolate recoil spectrum to table      bin 1: rate=0.081
values                                     bin 2: rate=0.098
# Assume spectrum zero outside data given  bin 3: rate=0.35
f_dRdE=interp1d(Er, dRdE)                 bin 4: rate=0.46
dRdE_matched=f_dRdE(E)                   bin 5: rate=0.29
Ri=TrapI(E[:,newaxis], Gi*dRdE_matched    bin 6: rate=0.22
[:,newaxis])                              bin 7: rate=0.18
                                           bin 8: rate=0.47
                                           bin 9: rate=0.84

for i,R in enumerate(Ri):
    print "bin 0: rate=1: .2g".format(i+1,R)

```

- [1] D. Harvey, R. Massey, T. Kitching, A. Taylor, and E. Tittley, *Science* **347**, 1462 (2015).
- [2] C. L. Bennett *et al.* (WMAP Collaboration), *Astrophys. J. Suppl. Ser.* **208**, 20 (2013).
- [3] P. A. R. Ade *et al.* (Planck Collaboration), *Astron. Astrophys.* **594**, A13 (2016).
- [4] J. Silk *et al.*, *Particle Dark Matter: Observations, Models and Searches* (Cambridge University Press, Cambridge, England, 2010).
- [5] E. Aprile *et al.* (XENON100 Collaboration), *Phys. Rev. D* **94**, 122001 (2016).
- [6] A. Tan *et al.* (PandaX-II Collaboration), *Phys. Rev. Lett.* **117**, 121303 (2016).
- [7] D. S. Akerib *et al.* (LUX Collaboration), *Phys. Rev. Lett.* **116**, 161301 (2016).
- [8] C. E. Aalseth *et al.* (CoGeNT Collaboration), *Phys. Rev. D* **88**, 012002 (2013).
- [9] R. Agnese *et al.* (SuperCDMS Collaboration), *Phys. Rev. Lett.* **112**, 041302 (2014).
- [10] G. Angloher *et al.*, *Eur. Phys. J. C* **72**, 1971 (2012).
- [11] R. Bernabei *et al.* (DAMA and LIBRA Collaborations), *Eur. Phys. J. C* **67**, 39 (2010).
- [12] J. D. Lewin and P. F. Smith, *Astropart. Phys.* **6**, 87 (1996).
- [13] S. Chang, A. Pierce, and N. Weiner, *J. Cosmol. Astropart. Phys.* **01** (2010) 006 (2010).
- [14] J. Fan, M. Reece, and L.-T. Wang, *J. Cosmol. Astropart. Phys.* **11** (2010) 042.
- [15] B. A. Dobrescu and I. Mocioiu, *J. High Energy Phys.* **11** (2006) 005.
- [16] A. L. Fitzpatrick, W. Haxton, E. Katz, N. Lubbers, and Y. Xu, [arXiv:1211.2818](https://arxiv.org/abs/1211.2818).
- [17] N. Anand, A. L. Fitzpatrick, and W. C. Haxton, *Phys. Rev. C* **89**, 065501 (2014).
- [18] A. L. Fitzpatrick, W. Haxton, E. Katz, N. Lubbers, and Y. Xu, *J. Cosmol. Astropart. Phys.* **02** (2013) 004.
- [19] D. Tucker-Smith and N. Weiner, *Phys. Rev. D* **64**, 043502 (2001).
- [20] G. Barelli, S. Chang, and C. A. Newby, *Phys. Rev. D* **90**, 094027 (2014).
- [21] See Supplemental Material at <http://link.aps.org/supplemental/10.1103/PhysRevD.96.042004> for XENON100 response table for the high energy recoil channel.
- [22] E. Aprile *et al.* (XENON100 Collaboration), *Astropart. Phys.* **35**, 573 (2012); **35**, 573 (2012).
- [23] E. Aprile *et al.* (XENON100 Collaboration), *Phys. Rev. Lett.* **109**, 181301 (2012).
- [24] E. Aprile *et al.* (XENON100 Collaboration), *Astropart. Phys.* **54**, 11 (2014).
- [25] E. Aprile *et al.* (XENON100 Collaboration), *J. Phys. G* **40**, 115201 (2013).
- [26] E. Aprile *et al.* (XENON100 Collaboration), *Phys. Rev. D* **88**, 012006 (2013).
- [27] E. Aprile *et al.* (XENON100 Collaboration), *J. Phys. G* **41**, 035201 (2014).
- [28] E. Aprile *et al.* (XENON100 Collaboration), *Phys. Rev. Lett.* **111**, 021301 (2013).
- [29] G. Cowan, K. Cranmer, E. Gross, and O. Vitells, *Eur. Phys. J. C* **71**, 1554 (2011); **73**, 2501(E) (2013).
- [30] E. Aprile *et al.* (XENON100 Collaboration), *Phys. Rev. Lett.* **107**, 131302 (2011).
- [31] E. Aprile *et al.* (XENON100 Collaboration), *Phys. Rev. D* **84**, 052003 (2011).
- [32] A. L. Read, in *Proceedings of the Workshop on Confidence Limits, CERN, Geneva, Switzerland, 2000* (CERN, Geneva, 2000), pp. 81–101, <http://weplib.cern.ch/abstract?CERN-OPEN-2000-205>.
- [33] K. Schneck *et al.* (SuperCDMS Collaboration), *Phys. Rev. D* **91**, 092004 (2015).
- [34] Z. Ahmed *et al.* (CDMS-II Collaboration), *Science* **327**, 1619 (2010).
- [35] D. Yu. Akimov *et al.* (ZEPLIN-III Collaboration), *Phys. Lett. B* **692**, 180 (2010).
- [36] E. Aprile *et al.* (XENON100 Collaboration), *Phys. Rev. D* **84**, 061101 (2011).
- [37] A. De Simone and T. Jacques, *Eur. Phys. J. C* **76**, 367 (2016).